THE JOURNAL OF PHYSICAL CHEMISTRY B

Feature Article

Cite This: J. Phys. Chem. B 2018, 122, 3023−3036

pubs.acs.org/JPCB

Live Cell Microscopy: A Physical Chemistry Approach

Somen Nandi,[†] Surajit Ghosh,[*,‡,§] and Kankan Bhattacharyya[*,∥]

[†]Department of Physical Chemistry, Indian Association for the Cultivation of Science, Jadavpur, Kolkata 700 032, India

[‡]Organic & Medicinal Chemistry Division, CSIR-Indian Institute of Chemical Biology, 4, Raja S. C. Mullick Road, Jadavpur, Kolkata, 700 032 West Bengal, India

[§]Academy of Scientific and Innovative Research (AcSIR), CSIR-Indian Institute of Chemical Biology Campus, 4 Raja S. C. Mullick Road, Jadavpur, Kolkata 700 032, India

[∥]Department of Chemistry, Indian Institute of Science Education and Research Bhopal, Bhopal, 462 066 Madhya Pradesh, India

ABSTRACT: Probing dynamics of intracellular components using physical chemistry techniques is a remarkable bottom-up approach for understanding the structures and functions of a biological cell. In this "Feature Article", we give an overview on local polarity, solvation, viscosity, acid−base property, red-ox processes (thiol−disulfide exchange), and gene silencing at selected intracellular components inside a live cell. Significant differences have been observed between cancer cells and their noncancer counterparts. We demonstrate that thiol−disulfide exchange, calcium oscillation, and gene silencing are manifested in time dependence of fluorescence intensity. We show that fluorescent gold nanoclusters may be used in drug delivery (e.g., doxorubicin) and selective killing of cancer cells. Further, we discuss dynamics and structural changes of DNA quadruplexes and i-motifs, induced by different external conditions (e.g., pH) and additives (e.g., K^+ and other target specific small molecules). We demonstrate that peptidomimetic analogues have high specificity over double-stranded DNA for binding with i-motifs and G-quadruplexes. These results may have significant biological implications.

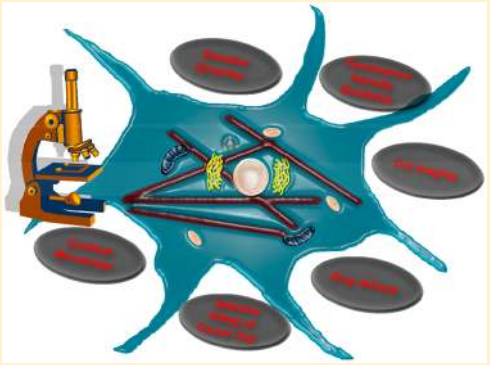

1. INTRODUCTION

Understanding intracellular components and their dynamics using a physical chemistry approach is challenging and, at the same time, highly rewarding. Capturing the dynamic complex environment inside a live functional cell is one of the longstanding goals of biophysical chemistry.[1] This has inspired a large number of recent studies on live cells *in vivo* using electron microscopy and super-resolution fluorescence microscopy.[1−11] In this article, we discuss the recent applications of a confocal microscope[12−14] to unravel various interesting phenomena occurring in a live cell. A biological cell is ∼50−100 times larger than the spatial resolution ($\lambda/2 \approx 200$ nm, Abbey limit) of a confocal microscope. Many fluorescent probes selectively localize in a specific region or organelle of a cell. The size of a fluorescent dye is in the order of ∼1 nm, and hence, they report on a region of radius ∼1 nm around the centroid of the probe.

We have earlier demonstrated that it is possible to probe different regions within a micelle of diameter ∼20 nm, immobilized in a triblock copolymer gel.[15] The immobilized micelles and gels (formed by pluoronic P123 and F127) contain a hydrophobic core of poly(propylene oxide) (PPO) and a hydrophilic corona of poly(ethylene oxide) (PEO) (Scheme 1A).[15] We determined translational diffusion coefficient (D_t) of fluorescent dyes in these gels by fluorescence correlation spectroscopy (FCS). According to the Stokes−Einstein relation, D_t is related to the size (radius, r_H) of the diffusing particle and local viscosity (η) as

$$D_t = \frac{k_B T}{6\pi\eta r_H} \quad (1)$$

In such a gel, the highly hydrophobic probe DCM (Scheme 1B) resides in the PPO core of the immobilized micelles, while the anionic and hydrophilic dye, coumarin 343 (C343, Scheme 1B), remains preferentially in the peripheral corona region, in contact with bulk water. The localization of the two probes over a small region is confirmed by red-edge excitation shift[16,17] of emission maxima.[15] In the immobilized micelles, D_t of both the dyes is much smaller than those in bulk water, indicating higher friction (i.e., viscosity). However, the magnitude of the increase in local viscosity in the gel, sensed by the two probes, is different. In F127 gel, D_t of DCM is about ∼300 times smaller than that in bulk water, which implies an about 300 times higher viscosity in the PPO core compared to that in bulk water.[15] D_t of C343 at the corona region in F127 gel is ∼20 times smaller than that in bulk water, indicating about 20-fold higher viscosity. Thus, compared to the corona, the local friction (viscosity) of the core is ∼15 times higher.[15]

Received: November 28, 2017
Revised: January 20, 2018
Published: February 1, 2018

Scheme 1. (A) Representative Picture of Micelle and Gel Formed by Pluoronic P123 and F127,[a] (B) Structure of Different Dyes, and (C) Labeling Reaction Scheme of Thiol Group of Proteins by CPM

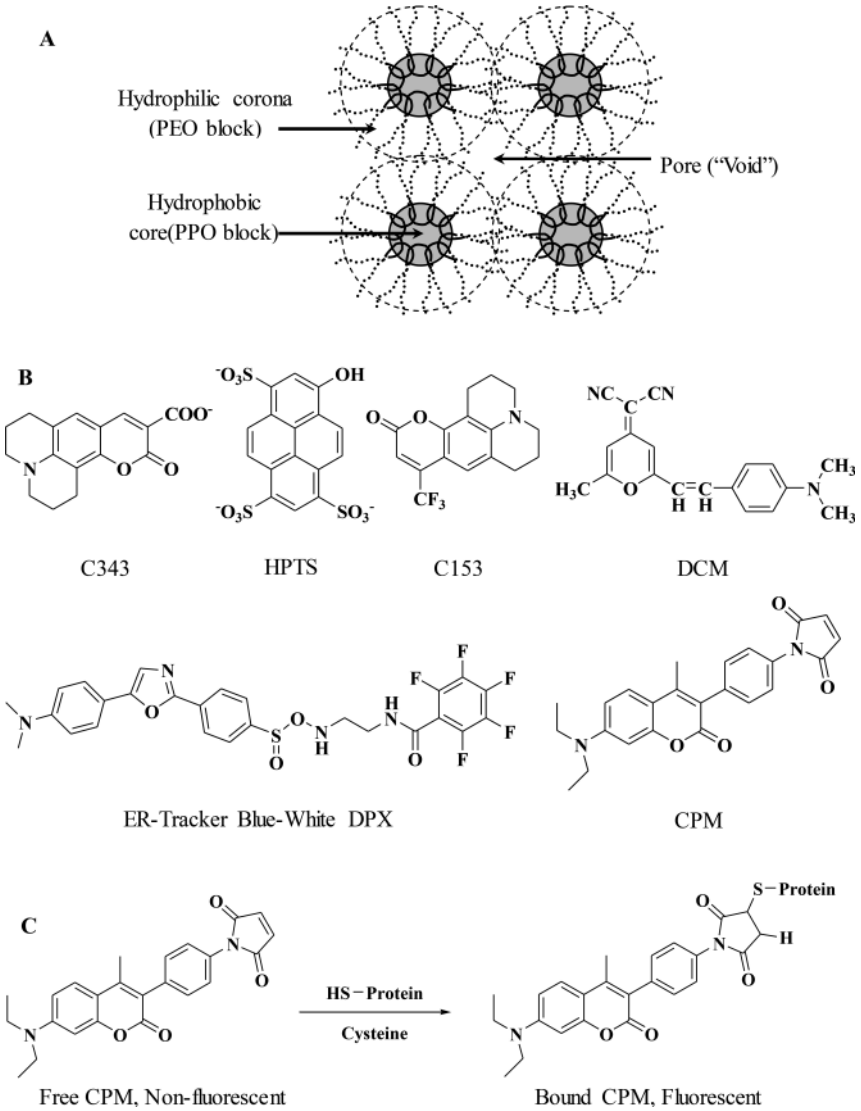

[a]Adapted with permission from ref 15. Copyright 2009 John Wiley and Sons.

Encouraged by this result, we have explored different regions of a live cell using nanometric fluorescent probes localized in specific locations of a cell. We have attempted to map local polarity, solvation, viscosity, acid−base property, red-ox processes (thiol−disulfide exchange), and gene silencing inside a live cell. In many cases, we have compared a cancer cell with its corresponding noncancer counterpart. We observed remarkable differences between cancer and noncancer cells. These results eventually prompted us to explore drug delivery and selective killing of cancer cells. In this article, we will discuss and highlight some of our recent findings.

2. PROBING SELECTED REGIONS OF A CELL

2.1. Local Solvation Environment at Selected Regions of a Live Cell. The local solvation environment (polarity or dielectric constant, ε) controls many complex biological processes or events.[18] For instance, transport of an ion or a proton (i.e., acid−base properties) or an electron requires stabilization of the charged and polar species, through solvation. There are many fluorescent probes whose fluorescence maximum depends on local polarity and solvation energy.[16−18]

The local polarity may be estimated by labeling different organelles of a live cell with a solvent sensitive fluorescent probe, recording fluorescence spectra under a confocal microscope and then comparing those with the emission spectra of the same dye in simple solvents.[19,20]

For a Chinese hamster ovary cell, we used the highly hydrophobic dye, DCM, for the cytoplasm region and DAPI (4′,6-diamidino-2-phenylindole), a DNA binding probe molecule, for the nucleus (where the DNAs reside).[21] We found that the emission maximum of DCM at cytoplasm resembles that in 2-propanol with a dielectric constant of ε = 15. On the contrary, for DAPI, which resides in the highly polar nucleus having a lot of ions (phosphate groups of DNA and counterion), the local polarity (emission maximum) is similar to that in 1:1 methanol−water mixture with ε = 65.[21]

Cytoplasm contains a large number of different organelles with different polarity. Using coumarin 153 (C153, Scheme 1B) as a fluorescent probe, we could visualize the cytoplasm, lipid droplets, and the nucleus of a Chinese hamster ovary cell

DOI: 10.1021/acs.jpcb.7b11689
J. Phys. Chem. B 2018, 122, 3023−3036

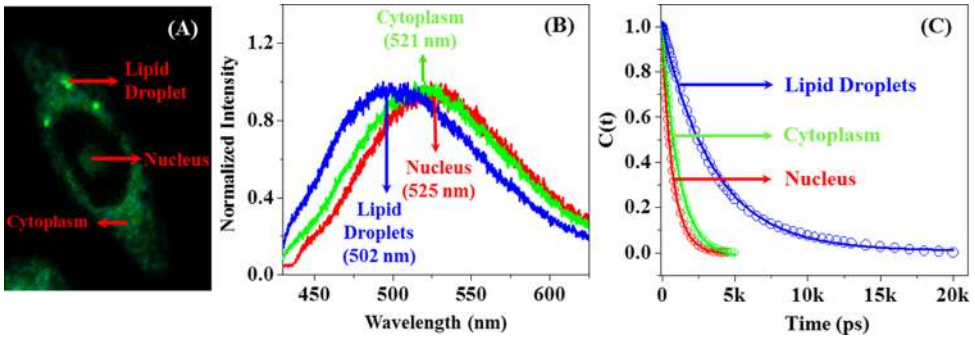

Figure 1. Chinese hamster ovary cell stained by C153 dye: (A) confocal image; (B) emission spectra; and (C) solvation dynamics (decays of solvent correlation function, $C(t)$).[22] Reprinted with permission from ref 22. Copyright 2013 American Chemical Society.

Table 1. Emission Maxima and Average Solvation Times ($\langle\tau_s\rangle$) in Different Regions of a Cell Stained by Different Fluorescent Probes[21,22,30−35]

system				
cell line	dye	region	emission maxima (nm)	$\langle\tau_s\rangle$[a] in ps
Chinese hamster ovary	CPM	membrane	476	500
	C153	cytoplasm	521	1100
	C153	nucleus	525	750
	C153	lipid droplets	502	3600
lung cancer (A549)	CPM	lipid droplets	476	1600
	C153	lipid droplets	495	3750
	CPM	cytoplasm	468	250
	DAPI	nucleus	460	300
	C153	cytoplasm	533	850
	ER tracker	endoplasmic reticulum	510	250
noncancer lung (WI38)	CPM	lipid droplets	472	800
	C153	lipid droplets	505	1700
	CPM	cytoplasm	474	400
	DAPI	nucleus	460	450
	C153	cytoplasm	525	1050
	ER tracker	endoplasmic reticulum	500	1000
breast cancer (MCF7)	CPM	mitochondria (peri-nuclear clustering)	470	1400
noncancer breast (MCF10A)	CPM	mitochondria (discrete)	475	850

[a] ± 50 ps.

(Figure 1).[22] The lipid droplets appear as bright dots (size ∼800 nm,[22] Figure 1A). The emission maxima of C153 in the nucleus, cytoplasm, and lipid droplets are observed at ∼525, 521, and 502 nm, respectively (Figure 1B). From the emission maxima of C153 in different solvents, the polarity (ε) of the nucleus, cytoplasm, and lipid droplets are estimated to be ∼26, 22, and 7, respectively.[22] In the case of the nucleus of the same cell, DAPI reports a much higher polarity ($\varepsilon = 65$)[21] because of the following reasons. DAPI localizes at the minor groove of the double-strand DNA, i.e., near the ions (phosphate groups of DNA and counterions).[23] C153 is a hydrophobic dye which resides in hydrophobic pockets inside the nucleus. The difference of polarity, which was reported by two dyes inside the nucleus of the same cell, reveals the variation of polarity inside a small part of the cell.

There is tremendous recent interest to understand solvation dynamics of "biological water" near a biological system, like protein, DNA, etc.[24−28] It is observed that solvation dynamics of biological water contain a component of ∼100−1000 times slower than that in bulk water (∼1 ps).[24−29] Until recently, biological waters were referred to as those in an aqueous solution of protein, DNA, or other biomolecules. The real biological water, however, resides inside a live cell.[30]

Using time-resolved confocal microscopy, we have been able to capture solvation dynamics of real biological water at different locations within a live cell (Table 1).[21,22,30−35] Though the ultrafast femtosecond component of solvation dynamics inside a live cell is still elusive, the experiment with picoseconds time resolution reveals a component in ∼100−1000 ps time scale in the live cell. In the case of Chinese hamster ovary cell stained by C153, the average solvation time $\langle\tau_s\rangle$ in various regions follows the order of lipid droplets (∼3600 ps) > cytoplasm (∼1100 ps) > nucleus (∼750 ps) (Figure 1C and Table 1).[22]

We found that the endoplasmic reticulum (ER) tracker dye, which localizes at the ER region, is itself a solvation probe. We have used this probe to monitor the solvation dynamics at the ER region of lung cells both in cancer (A549) as well as in noncancer (WI38) cells (Table 1).[35]

2.2. Lipid Droplets and Warburg Effect: Cancer vs Noncancer Cells. The accelerated rate of glycolysis in cancer cell and suppression of degradation of pyruvate leads to the formation of fat.[36−39] This results in proliferation of lipid droplets ("fat depot") in a cancer cell compared to a normal cell. This is referred to as the Warburg effect.[36−39] In fact, inhibition of the synthesis of lipid droplets have been suggested

DOI: 10.1021/acs.jpcb.7b11689
J. Phys. Chem. B 2018, 122, 3023−3036

to be a therapeutic cure of cancer.[39] We have compared the number of lipid droplets in a cancer cell with that in a normal (nonmalignant) cell.[31,32] The lipid droplets can be non-covalently labeled by C153 or nile red.[22,32] The lipid droplets appear as bright dots inside the cell (Figure 2). Comparing

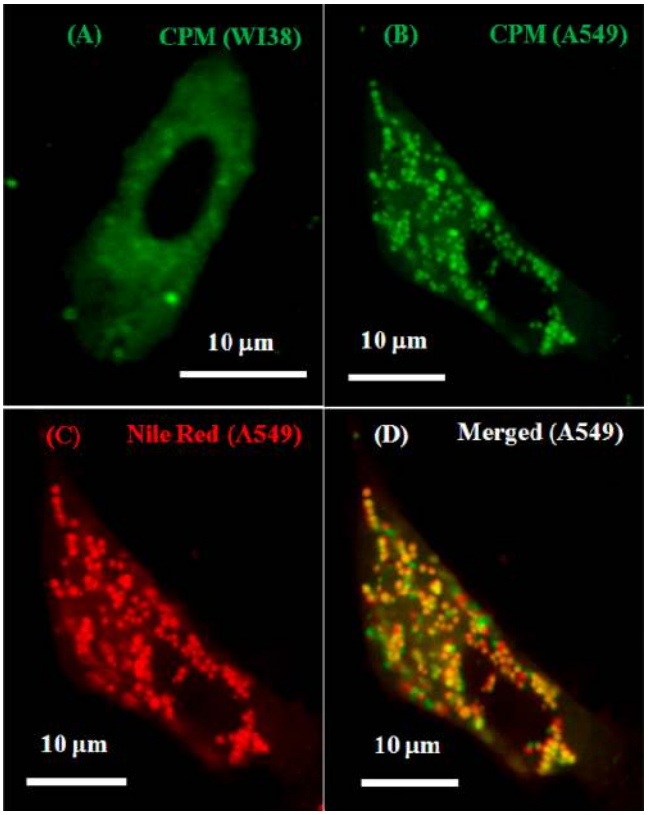

Figure 2. Lipid droplets inside lung cells: (A) WI38 labeled by CPM; (B) A549 labeled by CPM; (C) A549 labeled by nile red; and (D) merged image of (B) and (C).[31] Reprinted with permission from ref 31. Copyright 2015 American Chemical Society.

many cancer and noncancer cells, we found that the number of lipid droplets in a cell is a good diagnostic measure in identification of a cancer cell. In a normal cell, the number of such lipid droplets is below 15 (<15), while the number in a cancer cell is ∼50−100, i.e., about 5 to 10 times higher (Figure 2A,B).[31,32]

The lipid droplets are surrounded by a coat of a signaling protein (perilipin), which controls their degradation through autophagy.[37] We have observed that the lipid coat proteins containing a thiol (SH-protein) group may be covalently labeled by CPM (7-(diethylamino)-3-(4-maleimidylphenyl)-4-methylcoumarin, Scheme 1C).[31]

We have also studied solvation dynamics in lipid droplets using C153 and CPM as a solvation probe (Table 1). The results show that lipid droplets are marked by very slow solvation (∼800−3750 ps), and the emission maximum corresponds to a nonpolar environment (Table 1).[31,32] The preponderance of nonpolar lipid droplets inside a cancer cell may favor accumulation of hydrophobic molecules in lipid droplets.

2.3. Labeling of Mitochondria by CPM Dye. Mitochondria are widely known as the powerhouse of a cell. They play host to different biochemical processes which are important to the eukaryotic organisms involving metabolism, electron transport reactions, Krebs cycle, ion-channel signaling, etc. In order to monitor how these polar reactions are affected and the dynamics in the local environment of discrete and clustered mitochondria region of the normal breast cell (MCF10A) and breast cancer cell (MCF7), respectively, we have studied solvation dynamics at mitochondria.

We found that for human breast cells, the mitochondria may be labeled by CPM dye (Figures 3 and 4).[33] This indicates that the thiols at the mitochondria are the most reactive in human breast cells. The presence of CPM at the mitochondria is confirmed by a co-localization study with a mitochondria tracker (MT) dye. It is readily seen that the CPM dye localizes in the discrete mitochondria for the noncancerous breast cell (MCF10A) and at the peri-nuclear mitochondria for the cancer cell (MCF7) (Figures 3 and 4).[33] This suggests that the thiol groups at the peri-nuclear region are more reactive than the discrete mitochondria for the cancer cell.

The average solvation times for both of the cell-lines (∼850 ps for MCF10A and ∼1400 ps for MCF7, Table 1) reveal that the discrete mitochondria of a noncancer cell (MCF10A) exhibits almost ∼2-fold faster solvation dynamics as compared to that of a cancer cell (MCF7).[33] This demonstrates that CPM, bound to the thiol groups of various proteins in the mitochondrial clustered region, is less exposed to the solvent residing in the mitochondrial matrix and plays a vital role in regulating efflux and transport of ions.

2.4. Labeling of Cell Membrane by CPM Dye. In the case of the Chinese hamster ovary cell, we found that the thiols at the membrane are most reactive and one can specifically label the membrane region with CPM dye.[34] The thiols of the cell surface (i.e., exofacial thiols) play a very important role in transfection, and thus, the labeling of exofacial thiols is useful to study the processes occurring at the cell surface. We have

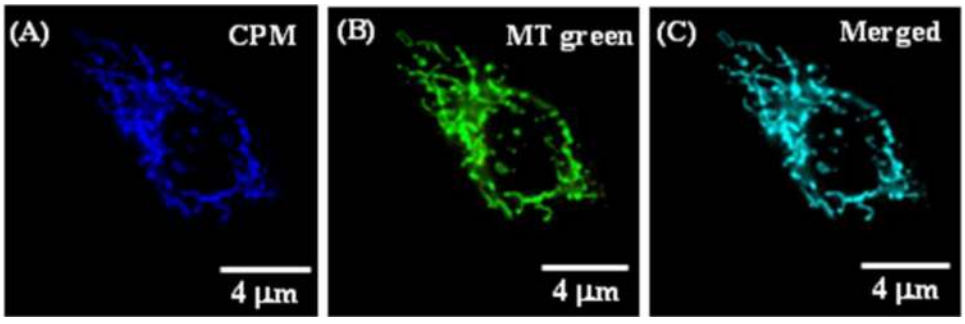

Figure 3. Co-localization of CPM with mitochondria tracker dye (mitotracker green, MT green) in discrete mitochondria of normal breast cell: (A) CPM, (B) MT-green, and (C) both.[33] Reprinted with permission from ref 33. Copyright 2015 American Chemical Society.

DOI: 10.1021/acs.jpcb.7b11689
J. Phys. Chem. B 2018, 122, 3023−3036

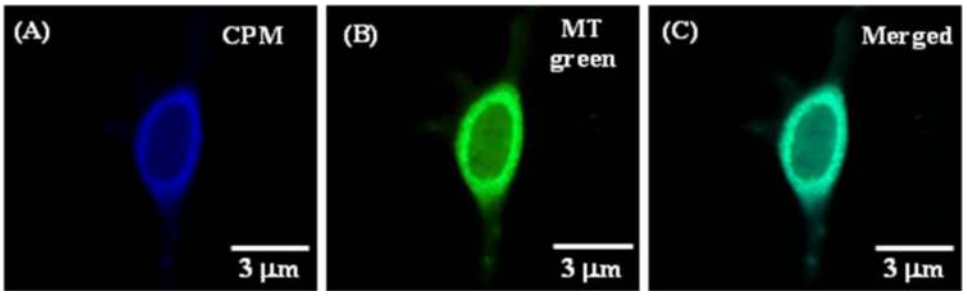

Figure 4. Co-localization of CPM with mitochondria tracker dye (MT) in peri-nuclear mitochondria region of breast cancer cell (MCF7).[33] Reprinted with permission from ref 33. Copyright 2015 American Chemical Society.

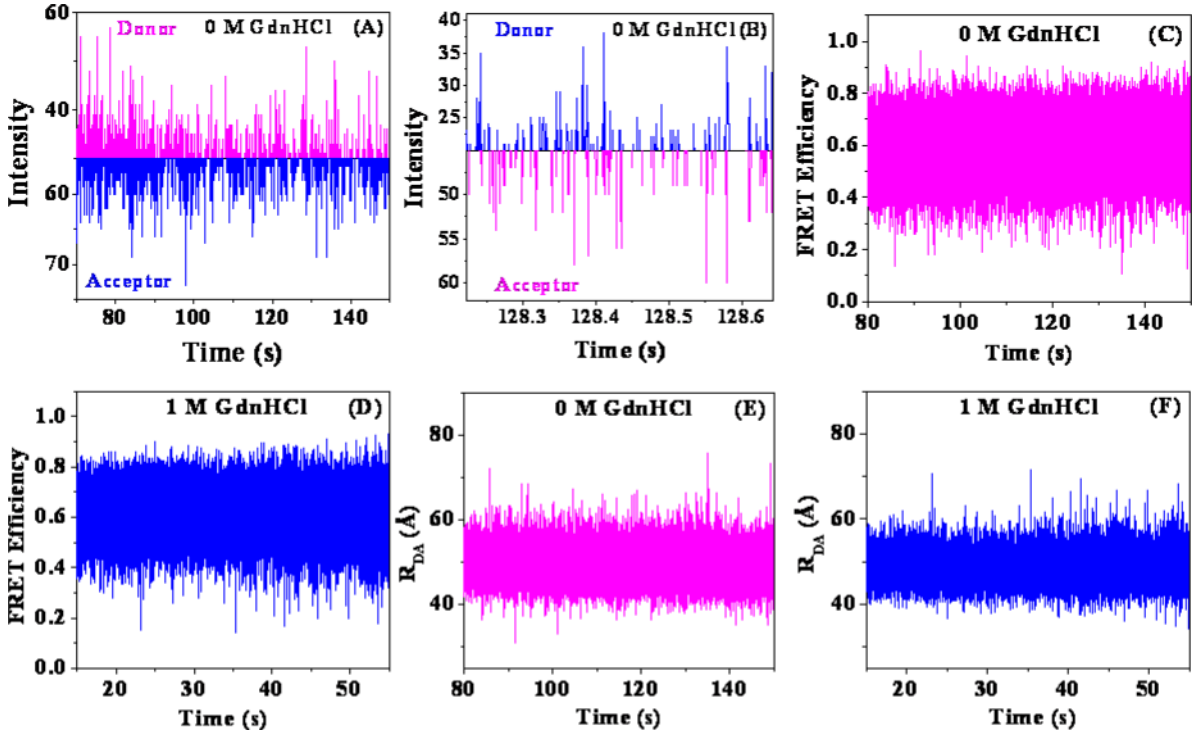

Figure 5. Photon bursts of the donor (D, EGFP, antigen) and acceptor (A, Alexa 594) bound to antibody: (A) full time scale; (B) expanded region. Variation of FRET efficiencies: (C) native; (D) denatured state (upon addition 1 M guanidine hydrochloride (GdnHCl)). Variation of R_{DA}: (E) in native; (F) denatured state (upon addition 1 M GdnHCl).[43] Adapted with permission from ref 43. Copyright 2015 Royal Society of Chemistry.

studied solvation dynamics at the membrane surface of the Chinese hamster ovary cell using CPM dye. It is observed that the time scale of solvation dynamics at the cell membrane is much shorter compared to those at the cytoplasm and the lipid droplets (Table 1).[34] This is attributed to the fact that the CPM dye, bound at the membrane of the surface, is exposed to bulk water and hence, exhibits faster dynamics.

2.5. Real-Time Monitoring of Intermittent Oscillations in Biological Systems. *2.5.1. sm-FRET Studies.* During many biochemical processes, a protein undergoes intermittent structural changes. Lu and co-workers detected intermittent coherence arising from structural fluctuation of an enzyme (HPPK) during its catalytic cycle.[40] Using single-molecule fluorescence resonance energy transfer (sm-FRET) technique, they found that the time scale of such oscillations is ~0.5 s.[40] They further examined the consequence of such structural fluctuations on enzyme kinetics for T4 lysozyme using the same technique.[41] They covalently labeled the noninterfering sites of the enzyme with a pair of donor (D) and acceptor (A).[41] This enabled them to monitor the changes in the point-to-point distance in real-time and, thus, they elucidated the role of the hinge-bending conformational motions of the active enzyme.[41] They demonstrated that the D−A distance (R_{DA}) and the donor fluorescence increased when the active sites remained open and decreased when they were closed.[41] They also detected time bunching effect. These results have revolutionized single molecule enzymology.[42]

Inspired by the beautiful experiments of Lu and co-workers, we studied sm-FRET in antigen−antibody complex (Figure 5).[43] In our case, the antigen (enhanced green fluorescent protein, EGFP) itself is a fluorescent molecule which acts as donor (D). We attached Alexa 594 (acceptor, A) covalently to the antibody. For the antigen−antibody complex the D−A distance (R_{DA}) fluctuates between ~30 and 80 Å in a time scale of seconds (Figure 5).[43] This demonstrates that in spite of the high specificity, the structure of the antigen−antibody complex is fluctuating.

We also applied sm-FRET to study growth (polymerization) and shrinkage (depolymerization) of microtubules. In this case, the donor is GFP, which is attached to an end-binding protein,

DOI: 10.1021/acs.jpcb.7b11689
J. Phys. Chem. B 2018, 122, 3023−3036

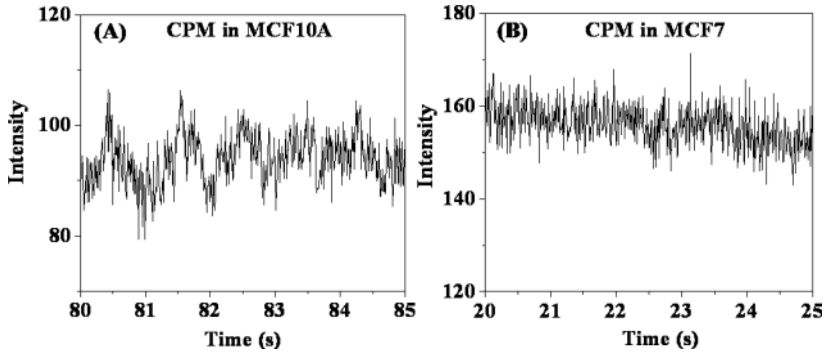

Figure 6. Fluorescence intensity vs time trajectories of CPM-labeled human breast cells. (A) Oscillations in normal cell (MCF10A) and (B) no oscillations in cancer cell (MCF7).[33] Reprinted with permission from ref 33. Copyright 2015 American Chemical Society.

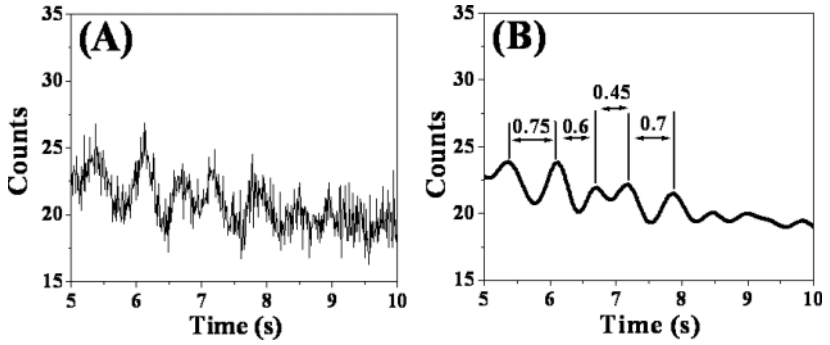

Figure 7. Intensity vs time trajectories. (A) CPM-labeled Chinese hamster ovary cell membrane, (B) corresponding FFT trace showing the half periods of oscillation.[34] Reprinted with permission from ref 34. Copyright 2014 American Chemical Society.

Mal3.[44] The acceptor is Alexa 568, which is linked to some of the tubulin monomer (1:11 ratio). Mal3 binds to the growing end of a microtubule only when it is polymerized. We observed FRET only when it is polymerized. Thus, the acceptor emission via FRET is observed only when microtubule is polymerized.[44] We determined the duration of the polymerized and depolymerized state of microtubule as ∼220 and ∼170 ms, respectively.[44] Even during the polymerized state the structure of microtubule is not rigid, and the D−A distance (R_{DA}) fluctuates between ∼28 and 80 Å with time.[44] It is also observed that the fluctuation of the microtubule is stopped when taxol is added.[45] This has implications in cancer because fluctuations in the microtubule lead to proliferation of cells, and taxol stops this in cancer cells by stabilizing the microtubule.

2.5.2. Red-Ox Fluctuations. We have tried to capture the thiol−disulfide exchange at different parts of a cell using CPM as a probe. CPM does not give fluorescence in the free state. CPM becomes strongly fluorescent only when it binds to a thiol group (Scheme 1C). We have demonstrated that the thiol−disulfide exchange manifests through oscillations in fluorescence intensities of the CPM dye at various locations of a biological cell, e.g., mitochondria,[33] membranes,[34] and lipid droplets.[31]

Interestingly, for the mitochondria, the cancer cell (MCF7) of human breast cells exhibits no oscillation (hence, red-ox inactivity), while the normal breast cells (MCF10A) display prominent oscillations in fluorescence intensity (Figure 6).[33] This may have implications in uncontrolled cell growth and highly inhibited apoptosis in cancer cells. For the Chinese hamster ovary cell membranes, the time scale of this oscillations is found to be ∼0.4−0.7 s (Figure 7).[34] Similar oscillations at the cell membrane have been recently reported from the study of membrane potential.[46] For the lipid droplets, the oscillation in a normal lung cell, WI38 (2.8 ± 0.7 s), is slower than those in the lung cancer cell, A549 (0.9 ± 0.3 s).[31]

2.5.3. Calcium Oscillations in ER of Lung Cells. ER in a cell controls the folding and modification of the secretory and membrane proteins and the fluctuation of intracellular calcium ions (Ca^{2+}).[47−49] The ER-tracker dye (ER-Tracker Blue-White DPX, Scheme 1B) is preferentially attached to the thiol groups. We monitored variation of fluorescence intensity with time of the probe to follow the calcium ion fluctuation causing open-closed structural changes of calcium binding proteins in a lung cell.[35] The lung cancer cell displays a prominent oscillation in the time scale of ∼2−6 s for a prolonged time period (150 s).[35] No such variation is observed in the case of the nonmalignant lung cell.[35] The larger amplitude and prominence oscillation observed in a lung cancer cell may arise from enhanced fluctuation in calcium ion (Ca^{2+}) concentration and, hence, may be a marker for the ER stress of a cancer cell.

2.6. Acid−Base Property inside a Cell. Acid−base property in a live cell and at the interfaces is a subject of great interest.[50,51] Tahara and co-workers have applied surface sum frequency to obtain the ratio of HA (a photoacid) and A^- of a pH indicator at water surface.[51] Hell and co-workers used fluorescent ratiometric pH indicator for the measurement of pH in endosomes inside a cell using super-resolution microscopy.[50] We have used a photoacid, pyranine (8-hydroxypyrene-1,3,6-trisulfonate, HPTS, Scheme 1B), to study the acid−base property inside a live cell.[52,53]

In the case of a photoacid (e.g., HPTS), the acid is created by photoexcitation.[52,53] The acid in the excited state (HA*) can undergo proton transfer (rate = $k_{PT} = 1/\tau_{PT}$) to form a geminate ion pair (A^-* and H^+, Scheme 2). The ion pair

DOI: 10.1021/acs.jpcb.7b11689
J. Phys. Chem. B 2018, 122, 3023−3036

Scheme 2. Proton Transfer Processes in the Excited State of a Photoacid, HA (e.g., HPTS)

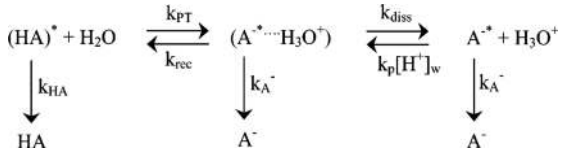

recombines to form HA* ($k_{rec} = 1/\tau_{rec}$). Thus, the effective acidity constant is $K_a^* = k_{PT}/k_{rec} = \tau_{rec}/\tau_{PT}$. Finally, the ion pair dissociates into solvent separated A^{-}* and H^+ (rate = $k_{diss} = 1/\tau_{diss}$, Scheme 2).

In the case of lung cells (both in cancerous and noncancerous cells), the probe HPTS localizes in the lysosome as determined by co-localization with a lysotracker dye (lysotracker yellow).[52] However, inside the Chinese hamster ovary cell, the same probe resides in the cytoplasm.[53]

In bulk water, the relative intensity of ~510 nm band (due to A^{-}* form) and ~450 nm band (due to HA*) in the emission spectrum of the photoacid, HPTS is about 20 (Figure 8).[52,53]

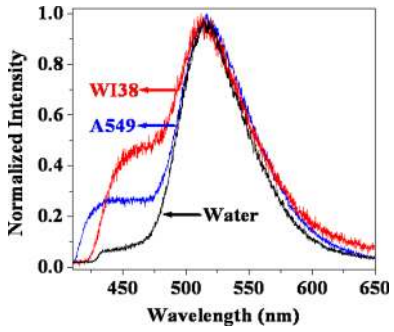

Figure 8. Fluorescence spectra of HPTS under a confocal microscope in bulk water and in lysosome of human lung cells.[52] Reprinted with permission from ref 52. Copyright 2015 American Chemical Society.

This ratio (I_{510}/I_{450}) dramatically decreases to ~1.4 ± 0.1 in the Chinese hamster ovary cell, ~2 ± 0.1 in the noncancer lung cell (WI38), and ~4 ± 0.1 in the lung cancer cell (A549) (Figure 8). In order to get a clear insight in the origin of this dramatic changes, we determined the rate constants, $k_{PT} = 1/\tau_{PT}$, $k_{rec} = 1/\tau_{rec}$, and $k_{diss} = 1/\tau_{diss}$, using time-resolved confocal microscopy (Table 2).[52,53]

The major changes in the ratio of I_{510}/I_{450} (relative population of A^{-}* and HA*) arise from the following three factors. First, the initial proton transfer process (τ_{PT}) slows down by a factor of ~8−10 and, thereby, increases the relative population of HA*. Second, inside the cell, the acidity constant, K_a*, reduces by a factor of ~2−3 and, thus, increases the relative amount of HA*. Third, within the cell, the rate of dissociation (k_{diss}) of the ion pair (producing free-A^{-}*) reduces by a factor of ~2−3, causing a reduction in relative population of A^{-}* (Table 2). This result demonstrates that variation of the relative ratio of HA and A^{-} emissions for an intracellular fluorescent probe may arise, mainly due to the changes in the rate of the elementary steps of proton transfer of the photoacid inside a cell (Scheme 2 and Table 2).[52,53]

2.7. Fluorescent Metal Nanoclusters: Cell Imaging and Implication in Drug Delivery. Gold nanoparticles having thousands of gold atoms are nonfluorescent. They have been used recently for cellular probing using Raman spectroscopy.[54−56] A metal nanocluster containing a few atoms (typically <30 atoms) often exhibits intense size dependent fluorescence.[57−78] Fluorescent metal clusters are photo stable and are found to be nontoxic to the live cells in most of the cases. The most common examples include noble metal nanoclusters comprising of gold (Au), silver (Ag), or platinum (Pt) atoms.[57−69] Dual metal nanoclusters,[74,75] consisting of both gold and silver, are also reported. Most recently, several groups also reported fluorescent nanoclusters of copper (Cu).[76−78]

According to the Jellium model, the emission frequency (ν_f) of a metal nanocluster is related to the size (radius, R) as,[57,58]

$$h\nu_f \approx \frac{E_f}{\sqrt[3]{N}} = \frac{E_f r_s}{R} \quad (2)$$

where E_f denotes the Fermi energy and r_s indicates Wigner−Seitz radius. From eq 2, it is evident that the number of metal atoms (N) in a nanocluster may be obtained from emission frequency. N may also be obtained from mass spectrometry.

2.7.1. Etching and Reaction of A Nanocluster inside A Cell: Higher Amount of Glutathione (GSH) in Cancer Cell. In bulk water, the highly reactive atoms in metal nanoclusters are protected by an organic capping agent. This organic capping agent may easily get replaced by molecules, like thiol containing peptides (e.g., glutathione etc.), or other small and large molecules/ligands inside a cell. In bulk water, the emission maximum of BSA-coated Au nanoclusters is at ~640 nm, which corresponds to N = 25 from eq 2 (i.e., Au_{25} core, Figure 9).[62] In the human breast cells, the emission maximum of this nanocluster exhibits a huge ~100 nm blue shift to ~530 nm, which corresponds to the Au_{13} core (Figure 9).[62] It is proposed that the glutathione (GSH) inside cancer cells removes the BSA capping agent and converts the Au_{25} into a Au_{13} core. Such etching of protein coated gold nanoclusters by GSH and replacement of protein by GSH *in vitro* is confirmed by MALDI mass spectrometry.[63]

2.7.2. Cell Imaging by Fluorescent Gold Nanoclusters. Figure 10 displays confocal microscopic pictures of fluorescent gold nanoclusters (Au-NCs)-labeled normal breast cell (MCF10A) and cancer breast cell (MCF7).[62] Evidently, gold nanoclusters invade the cancer cell (MCF7) and reside throughout the cytoplasm. On the contrary, the Au-NCs hardly go inside the noncancer cell (MCF10A) and

Table 2. Rates of Proton Transfer (k_{PT}), Recombination (k_{rec}), Dissociation (k_{diss}), and Acidity Constant (K_a) of HPTS in Bulk Water and inside Different Cell-Lines[52,53]

system	τ_{PT}[a] (ps)	τ_{rec}[a] (ps)	$K_a^* = \tau_{rec}/\tau_{PT}$	τ_{diss}[a] (ps)
water	5	7	1.4	50
normal lung cell (WI38)	40	25	0.62	120
lung cancer cell (A549)	40	30	0.75	80
Chinese hamster ovary cell	50	25	0.5	120

[a] ± 10%

DOI: 10.1021/acs.jpcb.7b11689
J. Phys. Chem. B 2018, 122, 3023−3036

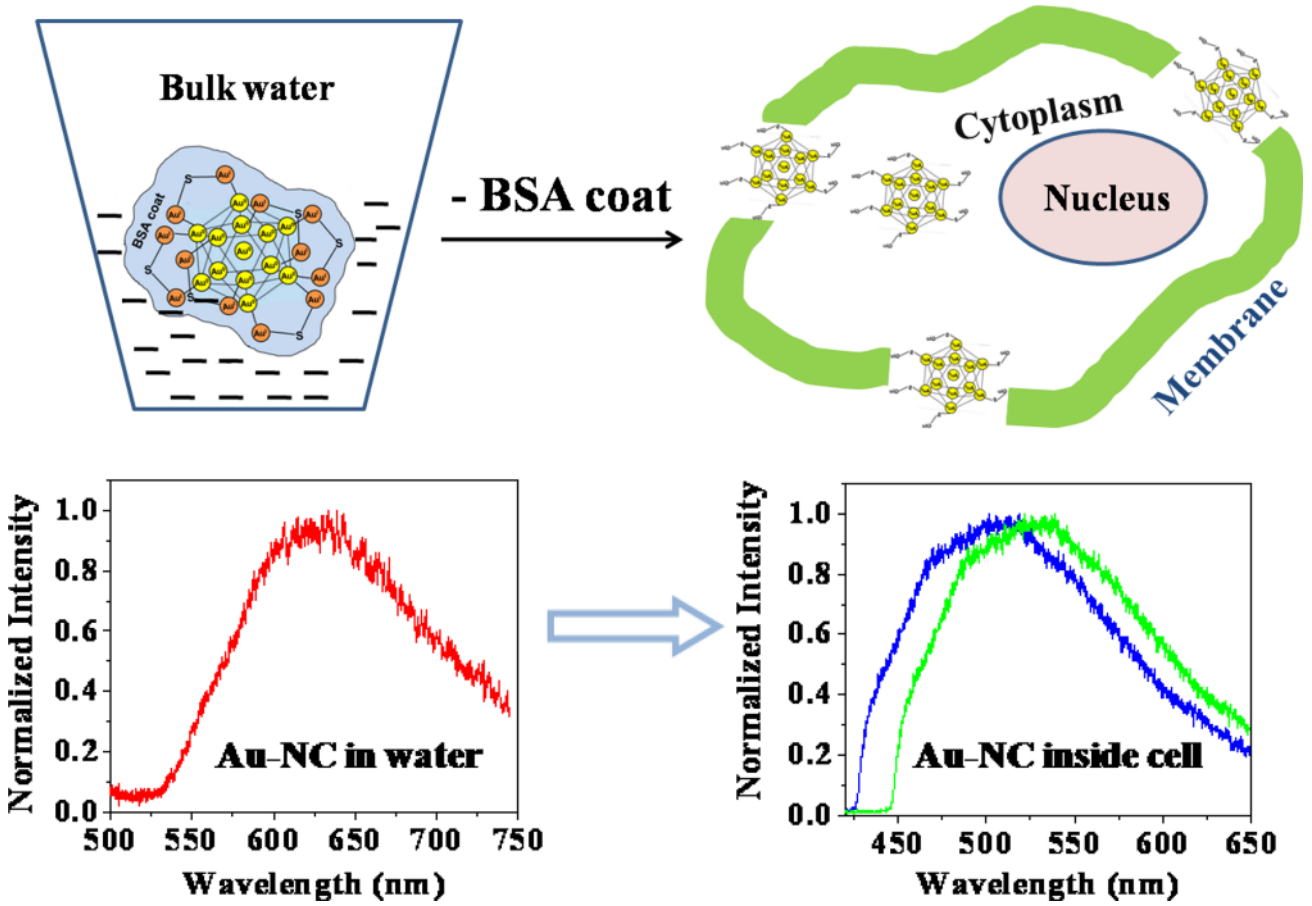

Figure 9. Etching of a BSA coated Au_{25} in bulk water to Au_{13} inside a cell.[62] Reprinted with permission from ref 62. Copyright 2014 American Chemical Society.

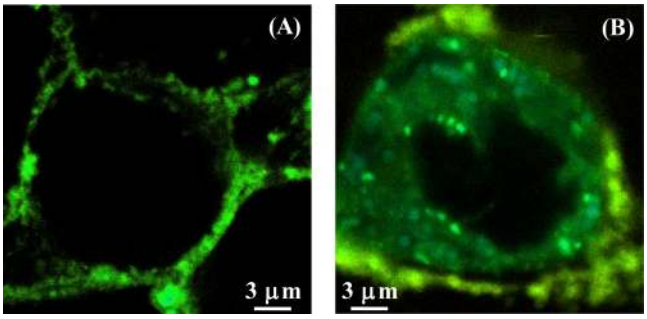

Figure 10. Confocal microscopic images of gold nanoclusters-labeled human breast cell: (A) nonmalignant cell; (B) cancer cell.[62] Reprinted with permission from ref 62. Copyright 2014 American Chemical Society.

preferentially localize at the membrane region of the cell. This is because of the strong affinity of gold atoms toward sulfur and the elevated level of glutathione (GSH) in a cancer cell.[79]

2.7.3. Fluorescent Metal Clusters in Delivery of Drug and Protein inside a Cell. Since Au-NCs enter inside the cancer cells and are unable to penetrate inside the noncancer cells of breast cells,[62] we used Au-NCs to deliver a cancer drug (doxorubicin).[63,64] We demonstrated that delivery of doxorubicin by gold nanoclusters causes selective killing of cancer cells, keeping noncancer cells intact.[63]

Since the protein, cytochrome c, is implicated in apoptosis, we explored the possibility of inducing apoptosis by delivering cytochrome c inside the cell using Au-NCs.[64] However, this approach was not successful and survival rate of the cancer cell was found to be greater.[64]

Usually, externally synthesized gold nanoclusters were added to the extra-cellular medium for live cell imaging. By this method, it was not possible to label the nucleus by externally generated gold nanoclusters. In order to image the nucleus, we have developed a new protocol to generate Au-NCs *in situ* inside a cell.[80] If $HAuCl_4$ (tetrachloroauric acid) is mixed with an imidazolium-based ionic liquid (e.g., 1-pentyl-3-methyl imidazolium bromide, [pmim][Br]),[81] a precipitate of [pmim]-$[AuCl_4]$ is formed with the cationic part ($[pmim]^+$) of the ionic liquid. From computer simulations, it has been shown that the ionic liquid, more precisely, the cationic $[pmim]^+$, binds to negatively charged DNA.[82] Since, in a cell, the DNAs reside in the nucleus, $[pmim][AuCl_4]$ ensures that a significant amount of Au-NCs are produced inside the nucleus. In this way, it becomes possible to clearly visualize the nucleus or, more precisely, the nucleolus of the cell.[80]

2.8. Local Viscosity at Selected Locations in a Live Cell. FCS may be applied to estimate the local viscosity in a live cell using eq 1 (Table 3). The basic strategy is to use a noncovalent fluorescent probe, which localizes in different parts of a cell and undergoes diffusion. In the case of the membrane of MCF10A, labeled by gold nanoclusters (Figure 10), it is more appropriate to use a model of two-dimensional diffusion (Saffman–Stokes–Einstein model),[83,84] which is written as

DOI: 10.1021/acs.jpcb.7b11689
J. Phys. Chem. B 2018, 122, 3023–3036

Table 3. Viscosity in Live Cells Obtained from FCS Using Eqs 1 and 3[22,62]

cell	region	viscosity
MCF7	cytoplasm	7 cP
	membrane	7.5×10^{-7} dyn-s/cm
MCF10A	membrane	0.8×10^{-7} dyn-s/cm
Chinese hamster ovary	cytoplasm	14.5 cP
	nucleus	13 cP
	lipid droplet	34 cP

$$D_{t,2D} = \frac{k_B T}{4\pi\eta_s}\left[\ln\left(\frac{\eta_s}{R\eta_t}\right) - 0.577\right] \quad (3)$$

where η_s is surface shear viscosity of the membrane. For MCF10A, we used the diffusion coefficient obtained from FCS as $D_{t,2D}$ and η_t = 1.02 cP (viscosity of culture medium). Then from eq 3, $\eta_s = 0.8 \times 10^{-7}$ dyn-s/cm (surface poise, SP) for the cell membrane (Table 3).[62]

For the Chinese hamster ovary cell, we used C153 as the probe to determine the viscosity at the cytoplasm, the nucleus, and lipid droplets. Tahara and co-workers developed a femtosecond fluorescence up-conversion microscope and studied the viscosity dependent ultrafast fluorescence dynamics of a fluorescent dye, malachite green in yeast cells.[85] From the decay time (2.2−2.4 ps) of the S_1 state of malachite green, they estimated the viscosity in the cytoplasm to be 5−6 cP.[85]

It is obvious that different regions of a cell have drastically different viscosities. If a probe is not localized in a particular region, one cannot directly apply the Stokes−Einstein equation (eq 1). In such cases, some authors prefer to follow a model of anomalous diffusion with polydispersity of the probe to account for the microscopic heterogeneity inside a cell.[86]

2.9. Stochastic Resonance in Gene Silencing. In this section, we discuss the mechanism of gene silencing by a short interfering RNA (siRNA) in a live cell. A cancer cell involves synthesis of various undesirable proteins. One possible therapy is to use a siRNA with ∼21−23 nucleotides to bind to the target gene and eventually silence the gene. Gene silencing is monitored by degradation of the target gene and also by translational inhibition of the resulting protein. A siRNA is double-stranded RNA. Inside the cell it uncoils and then binds to several proteins forming a RNA-induced silencing complex (RISC).[87,88] Uncoiled RNA guides the RISC to bind to the target gene in a highly specific manner. After binding to the target gene, the other proteins in the RISC (e.g., Ago, dicer, etc.) chop the gene.

The primary process of gene silencing is the recognition of the target gene inside the mRNA (containing typically thousands of genes). The process is analogous for the detection of a weak signal ("gene") in the presence of a large background noise. In the auditory perception of all animals, detection of such signal is achieved by a process called stochastic resonance. Stochastic resonance is defined as noise-assisted signal enhancement in a nonlinear system, and it is widely used in signal processing, communications, and control.[89−93] Transmission of sensory signal to the brain involves action potentials or spikes of neurons, and the signal is coded in the time intervals between the spikes.[89−93] Apart from the neuron network, the same algorithm has been applied to gene expression,[94,95] protein folding,[96−98] protein synthesis,[99] redox processes in cytochrome c,[100] NO reduction on platinum surface,[101] actin transport,[102] and fluctuation among different forms in supercooled water.[103] We had applied the same algorithm and detected dramatic differences in gene silencing between a cancer cell (MCF7) and a normal cell (MCF10A) of human breast cell.[104,105]

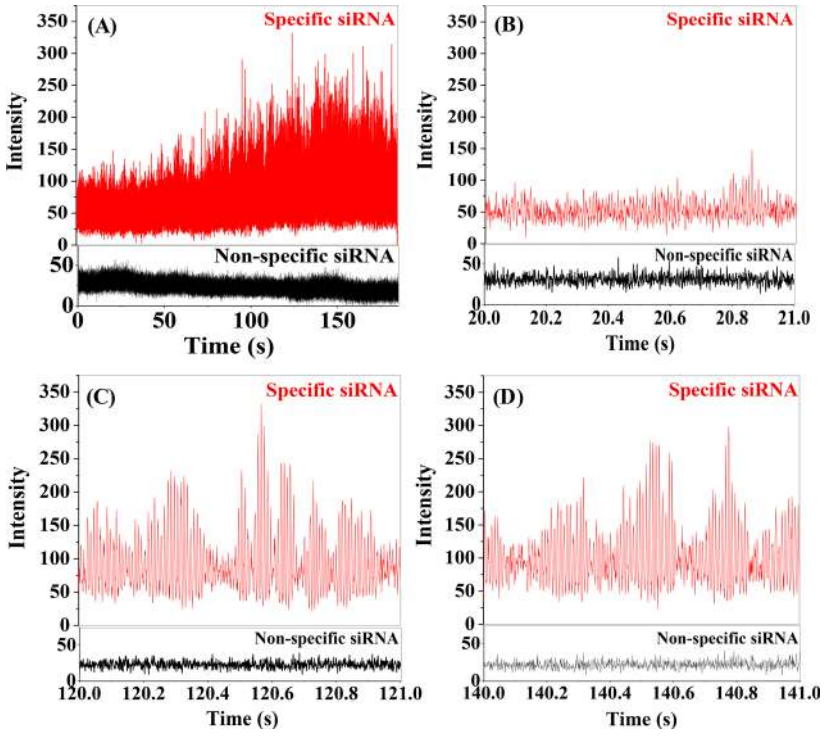

Figure 11. Fluorescence intensity time trajectories for specific (red) and nonspecific (black) siRNA in MCF7 cell.[104] Adapted with permission from ref 104. Copyright 2014 American Chemical Society.

DOI: 10.1021/acs.jpcb.7b11689
J. Phys. Chem. B 2018, 122, 3023−3036

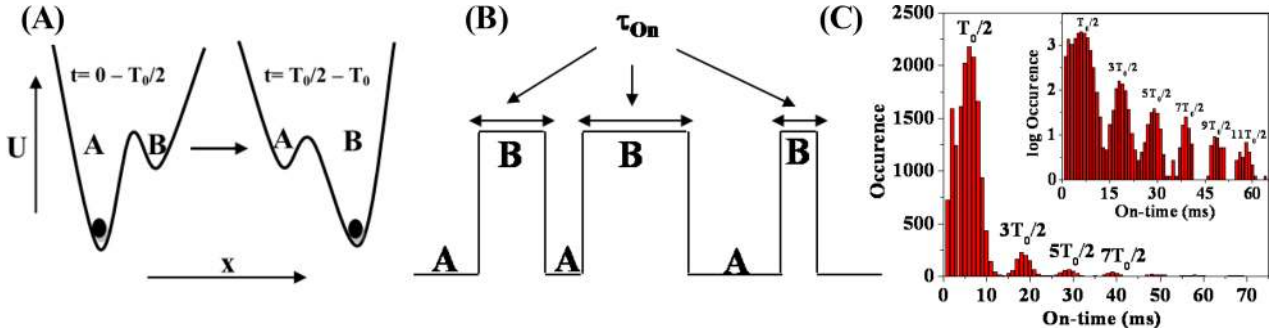

Figure 12. (A) Binding (A-to-B) and unbinding (B-to-A) of specific siRNA inside a cell. Distribution of on-time: (B) schematic representation and (C) histogram.[104] Reprinted with permission from ref 104. Copyright 2014 American Chemical Society.

2.9.1. Gene Silencing in a Breast Cancer Cell (MCF7). In our work, we focused on a specific siRNA which causes sequence-specific degradation of mRNA in MYH9 gene inside human breast cancer cell (MCF7).[104] As a control, we used a nonspecific siRNA. The number of nucleotides is same in the nonspecific and the specific siRNA. However, the only difference is in their homology, i.e., sequence of nucleotide bases. Because of the lack of complementarity, the nonspecific siRNA can neither bind to the target mRNA nor cause gene silencing.[104] Real-time PCR, using primers specific for MYH9 mRNA, revealed that the specific siRNA degrades about 88% mRNA and reduces synthesis of the protein, NMHC II-A, by ∼98% relative to the nonspecific siRNA.[104]

For confocal microscopy, a fluorophore (Alexa 488) is covalently attached to both sequences, specific and nonspecific siRNA. As shown in Figure 11, in the cancer cell MCF7, the fluorescence-labeled specific siRNA exhibits huge enhancement in fluorescence intensity on binding to its target mRNA. In contrast, the nonspecific siRNA, which cannot bind to mRNA, gives rise to low fluorescence intensity.

For the cancer cell, there is a long initial "dark" (low intensity) period of ∼70 s (Figure 11), which we attribute to the searching of the target gene by siRNA as it walks over mRNA. After this initial searching time, when the siRNA finds the target gene, there occurs a marked increase in fluorescence intensity (Figure 11A,C,D). This increase (i.e., "bright period") indicates binding of siRNA and is accompanied by many high-intensity spikes. It is reported that a repressor takes a similar time period (∼60 s) for searching a specific sequence in DNA.[94,95] Beyond ∼160 s, the high-intensity spikes disappear because of silencing of the gene. Hence, in a breast cancer cell, gene silencing takes place in ∼100 s time-scale.

No such bright period is observed at any time for specific siRNA in the culture medium. For the nonspecific siRNA, no high-intensity peaks are found in the culture medium, even inside the cell (Figure 11).

The most striking result is that all of the on-times (for the total of 16 273 periods for the breast cancer cell) are odd-integral multiples of a fundamental time period ($T_0/2$) of ∼5.5 ms. To rationalizes this striking result, we invoke the model of stochastic resonance as discussed by Longtin et al.[92] Stochastic resonance may be viewed as hopping between two wells in a bistable system described by double-well potential (Figure 12). For this, in the over damped limit, the Langevin equation is[89−93]

$$\dot{x} = -\frac{dU(x)}{dx} + \xi(t) + Q(\omega) \tag{4}$$

In eq 4, the random noise, $\xi(t)$, is strong enough to induce interwell hopping. The "weak" periodic signal, $Q(\omega)$, periodically varies relative to the energy of the two wells (as shown in Figure 12A). Thus, though the particle cannot be excited above the barrier by the "weak" signal, itself, it may create a bias for the excited particle to drop-in preferentially in the more stable well and makes the interwell hopping surprisingly regular.[94]

For gene silencing,[104] state A (low intensity) denotes unbound siRNA, whereas the state B (high intensity) indicates bound siRNA. Thus, the signal is due to high fluorescence intensity (from state B). A-to-B transition, i.e., binding of siRNA to target gene, involves finding the correct gene, i.e., nucleotide sequence. The reaction coordinate, x, comprises of distances of the ∼22 nucleotides of siRNA from the complementary nucleotides in mRNA. Many cycles of binding (hopping from A to B) or unbinding (B to A) precede successful gene silencing. Previously, Longtin et al.[92] proposed such an ABBA sequence remarkably similar to the binding-unbinding sequence.

We now examine the origin of the observed odd-integral multiple pattern of on-times as shown in Figure 12C. Let us define for binding, x is positive (>0). For a periodic noise, $Q(\omega) = Q_0 \sin \omega t$, magnitude of the periodic force Q (hence, x) is positive (implying binding, A-to-B) in the first half-period, $T_0/2$ ($\omega t = 0 - \pi$). For the second half period ($\omega t = \pi - 2\pi$), $x < 0$, which denotes unbinding (B-to-A). Probability of A−B transition is highest at $\omega t = \pi/2$. Conversely, unbinding (B-to-A) is most probable at $\omega t = 3\pi/2$. Thus, siRNA remains bound (i.e., on-time period) for a period of $T_0/2$ (from $\pi/2$ and $3\pi/2$).

If for some reason, unbinding does not occur at $\omega t = 3\pi/2$, another full cycle is needed and unbinding occurs at $3\pi/2 + 2\pi = 3T_0/2$. Similarly, the other "on-time," or "dwell-time" (Figure 12B) periods are 5, 7, 9,... times of $T_0/2$, that is an odd-integral multiple of $T_0/2$. In our case, $T_0/2 = 5.5 \pm 0.05$ ms. Similar residence times in the time scale of 0.3−5 ms were described for motion of a transcription factor on DNA.[97] Stochastic resonance behavior in gene expression had been reported earlier.[94,106,107]

The periodic driving force, $Q(\omega) = Q_0 \sin \omega t$, acts as a biological switch, which controls the binding of siRNA to mRNA. It appears that the periodic signal corresponds to periodical fluctuation in concentration of certain signaling molecules. It has been demonstrated that variation of chemical reagents by microfluidic devices causes similar oscillations in a synthetic gene.[107] The signaling molecules involved in gene silencing are yet to be identified. Complete elucidation of this important and complex issue is a fascinating unsolved question.

DOI: 10.1021/acs.jpcb.7b11689
J. Phys. Chem. B 2018, 122, 3023−3036

2.9.2. Gene Silencing in Noncancer Breast Cell (MCF10A). Kinetics of gene silencing in the normal breast cell (MCF10A) is entirely different. In MCF10A, the gene silencing is found to be a one-step irreversible process without repeated unbinding and rebinding. Thus, it would be highly interesting to find out the origin of the sinusoidal driving force, $Q(\omega) = Q_0 \sin \omega t$, which is only present in the cancer cell and is absent in the noncancer cell.

2.10. Structural Changes of DNA Quadruplexes and i-Motifs Induced by Different External Conditions and Additives. Under physiological conditions, a DNA remains in the double helical form. However, on addition of certain agents (e.g., K^+ ion or other small molecules), DNA may assume other structures, such as G-quadruplex[108−110] or i-motif.[111] Guanine (G)-rich sequences form quadruplexes in which four guanine bases form a square planar structure (guanine tetrad). The cytosine (C)-rich sequences form intercalated i-motifs at acidic pH.[111] The quadruplex reduces the activity of the enzyme telomerase. Telomerase preserves the length of telomeres and, thus, facilitates cell proliferation and, hence, is crucial in cancer. Hence, stabilization of DNA quadruplex is implicated in cancer therapy. Apart from the telomere region, the quadruplexes also control gene activity.

Dash et al. developed a carbazole derivative (bis-triazolylcarbazole, BTC) which induces quadruplex formation in proto-oncogene c-MYC and telomeric (h-TELO) G-rich DNA sequences.[108] Structure and dynamics of these quadruplexes were studied using sm-FRET and FCS. For sm-FRET, the DNA is labeled with a FRET donor and a FRET acceptor.[108] Excellent anticorrelation behavior of donor and acceptor fluorescence confirms sm-FRET. In the absence of K^+ ion, c-MYC exhibits two major peaks (at 0.6 and 0.4) in the FRET efficiency histogram plot with their corresponding donor−acceptor distances (R_{DA}) of ∼52 and 58 Å.[108] In the presence of K^+ ion, R_{DA} is found to be ∼43 Å. In absence of K^+ ion, addition of BTC leads to a very narrow distribution of FRET efficiency with R_{DA} = 41 Å. In the case of h-TELO, the R_{DA} distances are ∼55 (in K^+-free condition), 45 (in the presence of K^+ ion), 39 (in the presence of only BTC), and 41 Å (in the presence of BTC and K^+).[108] This is close to the size of folded G-quadruplexes (diameter ∼25 Å), after subtracting the lengths of the extra nucleotide and dye linkers presented in the dual-labeled sequences. The FCS studies indicate that there are ∼43 and 32% decreases in size of c-MYC and h-TELO, respectively, upon addition and subsequent binding of BTC. The rate constants for folding (end-to-end contact formation) and unfolding (dissociation) were also determined from FCS.[108]

Majima et al. investigated pH-induced i-motif DNA by FCS and sm-FRET.[111] Dash and co-workers used two bis-triazole-containing peptidomimetic ligands, which selectively bind the i-motif and G-quadruplex.[109] Free-BCL-2-C sequence exhibits a long donor−acceptor distance of R_{DA} = 50 Å at neutral pH (pH = 7). But, at the acidic pH (i.e., pH = 4.8), the BCL-2-C i-motif displays a rather short donor−acceptor distance (R_{DA} = 38 Å), indicating a compact structure.

3. CONCLUSION AND FUTURE OUTLOOK

A live cell is a dynamic complex machine undergoing many biochemical reactions and structural fluctuations. There are large numbers of intracellular components. These intracellular organelles have a specific task (functions) to maintain the cellular structure and various functions. Unraveling them in microscopic details is a fascinating issue because of the inherent theoretical and experimental challenges, and also their implications in opening up new avenues for therapy of various types of life-threatening diseases. Only a few of these phenomena are discussed and outlined in this article. This has already revealed many differences in various aspects between a cancer cell and the normal cell. Our concise overview on various intracellular components and implications of physical chemistry on a cell may be beneficial for further advancement of complex intracellular events. Usually, fluorescence lifetime imaging and FCS measurements are performed very easily under a confocal microscope. Tahara and co-workers introduced fluorescence lifetime correlation spectroscopy.[112] This might produce new knowledge on the various perspectives of biological cells. The time-resolved confocal microscopy is limited to picosecond time resolution. The femtosecond up-conversion microscope developed by Tahara and co-workers may enable to extend the time resolution to a femtosecond time scale.[85] The techniques described above basically require exogenous fluorescent dyes, and thus, these are the indirect methods to probe the intracellular environments of biological cells. Recently, Nakabayashi and co-workers assessed quantitatively the macromolecular crowding in a cell using multiconfocal Raman microscopy.[113] In this article, the force microscopy on cells[114,115] is not discussed, which is generating new knowledge on cells, in particular on molecular recognition at cell surfaces. FCS and lifetime measurement under super-resolution microscope are still difficult and may eventually pave the way for the ultimate space and time resolution for studying live cells.

AUTHOR INFORMATION

Corresponding Authors

*E-mail: sghosh@iicb.res.in; Fax: (91)-33-2473-2805.
*E-mail: kankan.bhattacharyya@gmail.com.

ORCID

Surajit Ghosh: 0000-0002-8203-8613
Kankan Bhattacharyya: 0000-0002-7463-3156

Notes

The authors declare no competing financial interest.

Biographies

Mr. Somen Nandi obtained his M.Sc. Degree from Indian Association for the Cultivation of Science (IACS) and has been pursuing Ph.D. research (Supervisor: Kankan Bhattacharyya) since 2014.

Dr. Surajit Ghosh obtained his Ph.D. at IIT Kanpur. After postdoctoral research at EMBL, Heidelberg, he joined CSIR-IICB as a faculty member in 2011.

Professor Kankan Bhattacharyya was a faculty member at IACS (1987−2016) and is the ex-Director (2009−2013). After retirement from IACS in 2016, he joined IISER Bhopal in 2016. He is a Senior Editor of the Journal of Physical Chemistry.

ACKNOWLEDGMENTS

S.N. gratefully acknowledges CSIR, India, for awarding fellowships. K.B. thanks DST JC Bose fellowship for financial research grants and supports. S.G. gives thanks to DBT, Government of India (BT/PR19159/NNT/1043/2016), for financial assistance.

DOI: 10.1021/acs.jpcb.7b11689
J. Phys. Chem. B 2018, 122, 3023−3036

REFERENCES

(1) Bhattacharyya, K.; Liu, G. Y.; Zanni, M. T. "New Physical Chemistry Insight" in Experimental Bio-Physical Chemistry. *J. Phys. Chem. B* **2017**, *121*, 6455−6455.

(2) Hashem, Y.; des Georges, A.; Fu, J.; Buss, S. N.; Jossinet, F.; Jobe, A.; Zhang, Q.; Liao, H. Y.; Grassucci, R. A.; Bajaj, C.; et al. High-Resolution Cryo-Electron Microscopy Structure of the *Trypanosoma brucei* Ribosome. *Nature* **2013**, *494*, 385−389.

(3) Smith, F. D.; Esseltine, J. L.; Nygren, P. J.; Veesler, D.; Byrne, D. P.; Vonderach, M.; Strashnov, I.; Eyers, C. E.; Eyers, P. A.; Langeberg, L. K.; et al. Local Protein Kinase A Action Proceeds through Intact Holoenzymes. *Science* **2017**, *356*, 1288−1293.

(4) Bieling, P.; Telley, I. A.; Surrey, T. A Minimal Midzone Protein Module Controls Formation and Length of Antiparallel Microtubule Overlaps. *Cell* **2010**, *142*, 420−432.

(5) Huang, J.; Roberts, A. J.; Leschziner, A. E.; Reck-Peterson, S. L. Lis1 Acts as A "Clutch" between the ATPase and Microtubule-Binding Domains of the Dynein Motor. *Cell* **2012**, *150*, 975−986.

(6) Lee, J. E.; Westrate, L. M.; Wu, H.; Page, C.; Voeltz, G. K. Multiple Dynamin Family Members Collaborate to Drive Mitochondrial Division. *Nature* **2016**, *540*, 139−143.

(7) Al Jord, A.; Lemaitre, A. I.; Delgehyr, N.; Faucourt, M.; Spassky, N.; Meunier, A. Centriole Amplification by Mother and Daughter Centrioles Differs in Multiciliated Cells. *Nature* **2014**, *516*, 104−107.

(8) Zhao, W. D.; Hamid, E.; Shin, W.; Wen, P. J.; Krystofiak, E. S.; Villarreal, S. A.; Chiang, H. C.; Kachar, B.; Wu, L. G. Hemi-Fused Structure Mediates and Controls Fusion and Fission in Live Cells. *Nature* **2016**, *534*, 548−552.

(9) Ou, H. D.; Phan, S.; Deerinck, T. J.; Thor, A.; Ellisman, M. H.; O'Shea, C. C. ChromEMT: Visualizing 3D Chromatin Structure and Compaction in Interphase and Mitotic Cells. *Science* **2017**, *357*, eaag0025.

(10) von Diezmann, A.; Shechtman, Y.; Moerner, W. E. Three-Dimensional Localization of Single Molecules for Super Resolution Imaging and Single-Particle Tracking. *Chem. Rev.* **2017**, *117*, 7244−7275.

(11) Giepmans, B. N.; Adams, S. R.; Ellisman, M. H.; Tsien, R. Y. The Fluorescent Toolbox for Assessing Protein Location and Function. *Science* **2006**, *312*, 217−224.

(12) Nie, S.; Chiu, D. T.; Zare, R. N. Probing Individual Molecules with Confocal Fluorescence Microscopy. *Science* **1994**, *266*, 1018−1021.

(13) Chowdhury, R.; Nandi, S.; Halder, R.; Jana, B.; Bhattacharyya, K. Structural Relaxation of Acridine Orange Dimer in Bulk Water and Inside Single Live Lung Cell. *J. Chem. Phys.* **2016**, *144*, 065101−1−8.

(14) Nandi, S.; Mondal, P.; Chowdhury, R.; Saha, A.; Ghosh, S.; Bhattacharyya, K. Amyloid Beta Peptides inside A Reconstituted Cell-Like Liposomal System: Aggregation, FRET, Fluorescence Oscillations and Solvation Dynamics. *Phys. Chem. Chem. Phys.* **2016**, *18*, 30444−30451.

(15) Ghosh, S.; Mandal, U.; Adhikari, A.; Bhattacharyya, K. Study of Diffusion of Organic Dyes in A Triblock Copolymer Micelle and Gel by Fluorescence Correlation Spectroscopy. *Chem. - Asian J.* **2009**, *4*, 948−954.

(16) Chattopadhyay, A.; Haldar, S. Dynamic Insight into Protein Structure Utilizing Red Edge Excitation Shift. *Acc. Chem. Res.* **2014**, *47*, 12−19.

(17) Lakowicz, J. R.; Keating-Nakamoto, S. Red-Edge Excitation of Fluorescence and Dynamic Properties of Proteins and Membranes. *Biochemistry* **1984**, *23*, 3013−3021.

(18) Lakowicz, J. R. *Principles of Fluorescence Spectroscopy*, 3rd ed.; Springer: New York, 2006; Chapters 3 and 24.

(19) Ghosh, C.; Nandi, S.; Bhattacharyya, K. Probing Micro-Environment of Lipid Droplets in A Live Breast Cell: MCF7 and MCF10A. *Chem. Phys. Lett.* **2017**, *670*, 27−31.

(20) Mohapatra, S.; Nandi, S.; Chowdhury, R.; Das, G.; Ghosh, S.; Bhattacharyya, K. Spectral Mapping of 3D Multi-Cellular Tumor Spheroids: Time-Resolved Confocal Microscopy. *Phys. Chem. Chem. Phys.* **2016**, *18*, 18381−18390.

(21) Sasmal, D. K.; Ghosh, S.; Das, A. K.; Bhattacharyya, K. Solvation Dynamics of Biological Water in A Single Live Cell under A Confocal Microscope. *Langmuir* **2013**, *29*, 2289−2298.

(22) Ghosh, S.; Chattoraj, S.; Mondal, T.; Bhattacharyya, K. Dynamics in Cytoplasm, Nucleus and Lipid Droplet of A Live CHO Cell: Time-Resolved Confocal Microscopy. *Langmuir* **2013**, *29*, 7975−7982.

(23) Pal, S. K.; Zhao, L. A.; Zewail, A. H. Water at DNA Surfaces: Ultrafast Dynamics in Minor Groove Recognition. *Proc. Natl. Acad. Sci. U. S. A.* **2003**, *100*, 8113−8118.

(24) Mondal, S.; Mukherjee, S.; Bagchi, B. Protein Hydration Dynamics: Much Ado about Nothing? *J. Phys. Chem. Lett.* **2017**, *8*, 4878−4882.

(25) Bagchi, B. *Water in Biological and Chemical Processes: From Structure and Dynamics to Function*; Cambridge University Press: Cambridge, U.K., 2013.

(26) Zhong, D.; Pal, S. K.; Zewail, A. H. Biological Water: A Critique. *Chem. Phys. Lett.* **2011**, *503*, 1−11.

(27) Bhattacharyya, K. Solvation Dynamics and Proton Transfer in Supramolecular Assemblies. *Acc. Chem. Res.* **2003**, *36*, 95−101.

(28) Bhattacharyya, K.; Bagchi, B. Slow Dynamics of Constrained Water in complex Geometries. *J. Phys. Chem. A* **2000**, *104*, 10603−10613.

(29) Bhattacharyya, K. Nature of Biological Water: A Femtosecond Study. *Chem. Commun.* **2008**, 2848−2857.

(30) Amin, M. A.; Nandi, S.; Mondal, P.; Mahata, T.; Ghosh, S.; Bhattacharyya, K. Physical Chemistry in A Single Live Cell: Confocal Microscopy. *Phys. Chem. Chem. Phys.* **2017**, *19*, 12620−12627.

(31) Chowdhury, R.; Amin, M. A.; Bhattacharyya, K. Intermittent Fluorescence Oscillations in Lipid Droplets in A Live Normal and Lung Cancer Cell: Time Resolved Confocal Microscopy. *J. Phys. Chem. B* **2015**, *119*, 10868−10875.

(32) Chowdhury, R.; Jana, B.; Saha, A.; Ghosh, S.; Bhattacharyya, K. Confocal Microscopy of Cytoplasmic Lipid Droplets in A Live Cancer Cell: Number, Polarity, Diffusion and Solvation Dynamics. *MedChemComm* **2014**, *5*, 536−539.

(33) Chattoraj, S.; Chowdhury, R.; Dey, S.; Jana, S. S.; Bhattacharyya, K. Role of Red-Ox Cycle in Structural Oscillations and Solvation Dynamics in the Mitochondria of A Live Cell. *J. Phys. Chem. B* **2015**, *119*, 8842−8851.

(34) Ghosh, S.; Chattoraj, S.; Bhattacharyya, K. Solvation Dynamics and Intermittent Oscillation of A Cell Membrane: Live Chinese Hamster Ovary Cell. *J. Phys. Chem. B* **2014**, *118*, 2949−2956.

(35) Ghosh, S.; Nandi, S.; Ghosh, C.; Bhattacharyya, K. Fluorescence Dynamics in the Endoplasmic Reticulum of A Live Cell: Time-Resolved Confocal Microscopy. *ChemPhysChem* **2016**, *17*, 2818−2823.

(36) Liberti, M. V.; Locasale, J. W. The Warburg Effect: How Does it Benefit Cancer Cells? *Trends Biochem. Sci.* **2016**, *41*, 211−218.

(37) Kaushik, S.; Cuervo, A. M. Degradation of Lipid Droplet-Associated Proteins by Chaperone-Mediated Autophagy Facilitates Lipolysis. *Nat. Cell Biol.* **2015**, *17*, 759−770.

(38) Banerjee, S.; Zare, R. N.; Tibshirani, R. J.; Kunder, C. A.; Nolley, R.; Fan, R.; Brooks, J. D.; Sonn, G. A. Diagnosis of Prostate Cancer by Desorption Electrospray Ionization Mass Spectrometric Imaging of Small Metabolites and Lipids. *Proc. Natl. Acad. Sci. U. S. A.* **2017**, *114*, 3334−3339.

(39) Bozza, P. T.; Viola, J. P. Lipid Droplets in Inflammation and Cancer. *Prostaglandins, Leukotrienes Essent. Fatty Acids* **2010**, *82*, 243−250.

(40) He, Y.; Li, Y.; Mukherjee, S.; Wu, Y.; Yan, H.; Lu, H. P. Probing Single-Molecule Enzyme Active-Site Conformational State Intermittent Coherence. *J. Am. Chem. Soc.* **2011**, *133*, 14389−14395.

(41) Lu, H. P. Revealing Time Bunching Effect in Single-Molecule Enzyme Conformational Dynamics. *Phys. Chem. Chem. Phys.* **2011**, *13*, 6734−6749.

(42) Lu, H. P. Enzymes in Coherent Motion. *Science* **2012**, *335*, 300−301.

DOI: 10.1021/acs.jpcb.7b11689
J. Phys. Chem. B 2018, 122, 3023−3036

(43) Bhunia, D.; Chowdhury, R.; Ghosh, S.; Bhattacharyya, K. Fluorescence Fluctuation of Antigen-Antibody Complex: Circular Dichroism, FCS and smFRET of Enhanced GFP and its Antibody. *Phys. Chem. Chem. Phys.* **2015**, *17*, 25250−25259.
(44) Mondal, P.; Chattoraj, S.; Chowdhury, R.; Bhunia, D.; Ghosh, S.; Bhattacharyya, K. Direct Observation of Growth and Shrinkage of Microtubules by Single Molecule Forster Resonance Energy Transfer. *Phys. Chem. Chem. Phys.* **2015**, *17*, 6687−6690.
(45) Ghosh, C.; Bhunia, D.; Ghosh, S.; Jana, B.; Ghosh, S.; Bhattacharyya, K. Fluorescence Probing of Fluctuating Microtubule using a Covalent Fluorescent Probe: Effect of Taxol. *Chemistry Select* **2016**, *1*, 1841−1847.
(46) Domnisoru, C.; Kinkhabwala, A. A.; Tank, D. W. Membrane Potential Dynamics of Grid Cells. *Nature* **2013**, *495*, 199−204.
(47) Wang, M.; Kaufman, R. J. The Impact of the Endoplasmic Reticulum Protein-Folding Environment on Cancer Development. *Nat. Rev. Cancer* **2014**, *14*, 581−597.
(48) Dupont, G.; Combettes, L.; Bird, G. S.; Putney, J. W. Calcium Oscillations. *Cold Spring Harbor Perspect. Biol.* **2011**, *3*, a004226−1−18.
(49) Anelli, T.; Alessio, M.; Bachi, A.; Bergamelli, L.; Bertoli, G.; Camerini, S.; Mezghrani, A.; Ruffato, E.; Simmen, T.; Sitia, R. Thiol-Mediated Protein Retention in the Endoplasmic Reticulum: The Role of Erp 44. *EMBO J.* **2003**, *22*, 5015−5022.
(50) Richardson, D. S.; Gregor, C.; Winter, F. R.; Urban, N. T.; Sahl, S. J.; Willig, K. I.; Hell, S. W. SRpHi Ratiometric pH Biosensors for Super-Resolution Microscopy. *Nat. Commun.* **2017**, *8*, No. 577, DOI: 10.1038/s41467-017-00606-4.
(51) Yamaguchi, S.; Bhattacharyya, K.; Tahara, T. Acid-Base Equilibrium at an Aqueous Interface: pH Spectrometry by Heterodyne-Detected Electronic Sum Frequency Generation. *J. Phys. Chem. C* **2011**, *115*, 4168−4173.
(52) Chowdhury, R.; Saha, A.; Mandal, A. K.; Jana, B.; Ghosh, S.; Bhattacharyya, K. Excited State Proton Transfer in the Lysosome of Live Lung Cells: Normal and Cancer Cells. *J. Phys. Chem. B* **2015**, *119*, 2149−2156.
(53) Sen Mojumdar, S.; Chowdhury, R.; Mandal, A. K.; Bhattacharyya, K. In What Time Scale Proton Transfer Takes Place in A Live CHO Cell? *J. Chem. Phys.* **2013**, *138*, 215102−1−9.
(54) Drescher, D.; Traub, H.; Büchner, T.; Jakubowski, N.; Kneipp, J. Properties of In Situ Generated Gold Nanoparticles in the Cellular Context. *Nanoscale* **2017**, *9*, 11647−11656.
(55) Jin, Q.; Li, M.; Polat, B.; Paidi, S. K.; Dai, A.; Zhang, A.; Pagaduan, J. V.; Barman, I.; Gracias, D. H. Mechanical Trap Surface-Enhanced Raman Spectroscopy for Three-Dimensional Surface Molecular Imaging of Single Live Cells. *Angew. Chem., Int. Ed.* **2017**, *56*, 3822−3826.
(56) Pandey, R.; Paidi, S. K.; Valdez, T. A.; Zhang, C.; Spegazzini, N.; Dasari, R. R.; Barman, I. Noninvasive Monitoring of Blood Glucose with Raman Spectroscopy. *Acc. Chem. Res.* **2017**, *50*, 264−272.
(57) Zheng, J.; Nicovich, P. R.; Dickson, R. M. Highly Fluorescent Noble-Metal Quantum Dots. *Annu. Rev. Phys. Chem.* **2007**, *58*, 409−431.
(58) Choi, S.; Dickson, R. M.; Yu, J. Developing Luminescent Silver Nanodots for Biological Applications. *Chem. Soc. Rev.* **2012**, *41*, 1867−1891.
(59) Cui, H.; Hu, D.; Zhang, J.; Gao, G.; Chen, Z.; Li, W.; Gong, P.; Sheng, Z.; Cai, L. Gold Nanoclusters−Indocyanine Green Nanoprobes for Synchronous Cancer Imaging, Treatment, and Real-Time Monitoring Based on Fluorescence Resonance Energy Transfer. *ACS Appl. Mater. Interfaces* **2017**, *9*, 25114−25127.
(60) Wang, C.; Chen, J.; Talavage, T.; Irudayaraj, J. Gold Nanorod/Fe_3O_4 Nanoparticle "Nano-Pearl-Necklaces" for Simultaneous Targeting, Dual-Mode Imaging, and Photothermal Ablation of Cancer Cells. *Angew. Chem., Int. Ed.* **2009**, *48*, 2759−2763.
(61) Nair, L. V.; Nazeer, S. S.; Jayasree, R. S.; Ajayaghosh, A. Fluorescence Imaging Assisted Photodynamic Therapy Using Photosensitizer-Linked Gold Quantum Clusters. *ACS Nano* **2015**, *9*, 5825−5832.
(62) Chattoraj, S.; Bhattacharyya, K. Fluorescent Gold Nano-Cluster inside A Live Breast Cell: Etching and Higher Uptake in Cancer Cell. *J. Phys. Chem. C* **2014**, *118*, 22339−22346.
(63) Chattoraj, S.; Amin, M. A.; Jana, B.; Mohapatra, S.; Ghosh, S.; Bhattacharyya, K. Selective Killing of Breast Cancer Cells by Doxorubicin Loaded Fluorescent Gold Nano-Cluster: Confocal Microscopy and FRET. *ChemPhysChem* **2016**, *17*, 253−259.
(64) Chattoraj, S.; Amin, M. A.; Bhattacharyya, K. Cytochrome c-Capped Fluorescent Gold Nanoclusters: Imaging of Live Cells and Delivery of Cytochrome c. *ChemPhysChem* **2016**, *17*, 2088−2095.
(65) Chattoraj, S.; Amin, M. A.; Mohapatra, S.; Ghosh, S.; Bhattacharyya, K. Cancer Cell Imaging by In Situ Generated Gold Nano-Clusters. *ChemPhysChem* **2016**, *17*, 61−68.
(66) Chaudhari, K.; Xavier, P. L.; Pradeep, T. Understanding the Evolution of Luminescent Gold Quantum Clusters in Protein Templates. *ACS Nano* **2011**, *5*, 8816−8827.
(67) Xu, Y.; Sherwood, J.; Qin, Y.; Crowley, D.; Bonizzoni, M.; Bao, Y. The Role of Protein Characteristics in the Formation and Fluorescence of Au Nanoclusters. *Nanoscale* **2014**, *6*, 1515−1524.
(68) Chen, Y. S.; Kamat, P. V. Glutathione-Capped Gold Nanoclusters as Photosensitizers. Visible Light-Induced Hydrogen Generation in Neutral Water. *J. Am. Chem. Soc.* **2014**, *136*, 6075−6082.
(69) Stamplecoskie, K. G.; Kamat, P. V. Size-Dependent Excited State Behavior of Glutathione-Capped Gold Clusters and Their Light-Harvesting Capacity. *J. Am. Chem. Soc.* **2014**, *136*, 11093−11099.
(70) Badugu, R.; Szmacinski, H.; Ray, K.; Descrovi, E.; Ricciardi, S.; Zhang, D.; Chen, J.; Huo, Y.; Lakowicz, J. R. Fluorescence Spectroscopy with Metal−Dielectric Waveguides. *J. Phys. Chem. C* **2015**, *119*, 16245−16255.
(71) Aly, S. M.; AbdulHalim, L. G.; Besong, T. M.; Soldan, G.; Bakr, O. M.; Mohammed, O. F. Ultrafast Static and Diffusion-Controlled Electron Transfer at Ag_{29} Nanocluster/Molecular Acceptor Interfaces. *Nanoscale* **2016**, *8*, 5412−5416.
(72) Tanaka, S.; Miyazaki, J.; Tiwari, D. K.; Jin, T.; Inouye, Y. Fluorescent Platinum Nanoclusters: Synthesis, Purification, Characterization, and Application to Bioimaging. *Angew. Chem., Int. Ed.* **2011**, *50*, 431−435.
(73) Tiwari, J. N.; Nath, K.; Kumar, S.; Tiwari, R. N.; Kemp, K. C.; Le, N. H.; Youn, D. H.; Lee, J. S.; Kim, K. S. Stable Platinum Nanoclusters on Genomic DNA-Graphene Oxide with a High Oxygen Reduction Reaction Activity. *Nat. Commun.* **2013**, *4*, No. 2221, DOI: 10.1038/ncomms3221.
(74) Chowdhury, M. H.; Chakraborty, S.; Lakowicz, J. R.; Ray, K. Feasibility of Using Bimetallic Plasmonic Nanostructures to Enhance the Intrinsic Emission of Biomolecules. *J. Phys. Chem. C* **2011**, *115*, 16879−16891.
(75) Wang, Y.; Su, H.; Xu, C.; Li, G.; Gell, L.; Lin, S.; Tang, Z.; Häkkinen, H.; Zheng, N. An Intermetallic $Au_{24}Ag_{20}$ Superatom Nanocluster Stabilized by Labile Ligands. *J. Am. Chem. Soc.* **2015**, *137*, 4324−4327.
(76) Barthel, M. J.; Angeloni, I.; Petrelli, A.; Avellini, T.; Scarpellini, A.; Bertoni, G.; Armirotti, A.; Moreels, I.; Pellegrino, T. Synthesis of Highly Fluorescent Copper Clusters Using Living Polymer Chains as Combined Reducing Agents and Ligands. *ACS Nano* **2015**, *9*, 11886−11897.
(77) Ghosh, S.; Das, N. K.; Anand, U.; Mukherjee, S. Photostable Copper Nanoclusters: Compatible Förster Resonance Energy-Transfer Assays and A Nanothermometer. *J. Phys. Chem. Lett.* **2015**, *6*, 1293−1298.
(78) Liu, C.; Yang, B.; Tyo, E.; Seifert, S.; DeBartolo, J.; von Issendorff, B.; Zapol, P.; Vajda, S.; Curtiss, L. A. Carbon Dioxide Conversion to Methanol over Size-Selected Cu_4 Clusters at Low Pressures. *J. Am. Chem. Soc.* **2015**, *137*, 8676−8679.
(79) Russo, A.; DeGraff, W.; Friedman, N.; Mitchell, J. B. Selective Modulation of Glutathione Levels in Human Normal versus Tumor Cells and Subsequent Differential Response to Chemotherapy Drugs. *Cancer Res.* **1986**, *46*, 2845−2848.

DOI: 10.1021/acs.jpcb.7b11689
J. Phys. Chem. B 2018, 122, 3023−3036

(80) Chattoraj, S.; Amin, M. A.; Mohapatra, S.; Ghosh, S.; Bhattacharyya, K. Cancer Cell Imaging by In Situ Generated Gold Nano-clusters. *ChemPhysChem* **2016**, *17*, 61−68.
(81) Nandi, S.; Parui, S.; Halder, R.; Jana, B.; Bhattacharyya, K. Interaction of Proteins with Ionic Liquid, Alcohol and DMSO and In Situ Generation of Gold Nano-Clusters in A Cell. *Biophys. Rev.* **2017**, *2017*, 1−12, DOI: 10.1007/s12551-017-0331-1.
(82) Chandran, A.; Ghoshdastidar, D.; Senapati, S. Groove Binding Mechanism of Ionic Liquids: A Key Factor in Long-Term Stability of DNA in Hydrated Ionic Liquids? *J. Am. Chem. Soc.* **2012**, *134*, 20330−20339.
(83) Saffman, P. G.; Delbruck, M. Brownian Motion in Biological Membranes. *Proc. Natl. Acad. Sci. U. S. A.* **1975**, *72*, 3111−3113.
(84) Hormel, T. T.; Kurihara, S. Q.; Brennan, M. K.; Wozniak, M. C.; Parthasarathy, R. Measuring Lipid Membrane Viscosity Using Rotational and Translational Probe Diffusion. *Phys. Rev. Lett.* **2014**, *112*, 188101.
(85) Fujino, T.; Hirota, K.; Ohta, K.; Tahara, T. In-Cell Viscosity Measurement Using a Fluorescence Up-conversion Microscope. *Chem. Lett.* **2008**, *37*, 1240−1241.
(86) Kalwarczyk, T.; Kwapiszewska, K.; Szczepanski, K.; Sozanski, K.; Szymanski, J.; Michalska, B.; Patalas-Krawczyk, P.; Duszynski, J.; Holyst, R. Apparent Anomalous Diffusion in the Cytoplasm of Human Cells: The Effect of Probes' Polydispersity. *J. Phys. Chem. B* **2017**, *121*, 9831−9837.
(87) Meister, G.; Tuschl, T. Mechanism of Gene Silencing by Double Stranded RNA. *Nature* **2004**, *431*, 343−349.
(88) Carthew, R. W.; Sontheimer, E. J. Origins and Mechanisms of miRNAs and siRNAs. *Cell* **2009**, *136*, 642−655.
(89) Sancristóbal, B.; Rebollo, B.; Boada, P.; Sanchez-Vives, M. V.; Garcia-Ojalvo, J. Collective Stochastic Coherence in Recurrent Neuronal Networks. *Nat. Phys.* **2016**, *12*, 881−887.
(90) Wiesenfeld, K.; Moss, F. Stochastic Resonance and Benefits of Noise: From Ice Ages to Crayfish and SQUIDs. *Nature* **1995**, *373*, 33−36.
(91) Levin, J. E.; Miller, J. P. Broadband Neural Encoding in the Cricket Cereal Sensory System Enhanced by Stochastic Resonance. *Nature* **1996**, *380*, 165−168.
(92) Longtin, A.; Bulsara, A.; Moss, F. Time-Interval Sequences in Bistable Systems and the Noise-Induced Transmission of Information by Sensory Neurons. *Phys. Rev. Lett.* **1991**, *67*, 656−659.
(93) Gammaitoni, L.; Hänggi, P.; Jung, P.; Marchesoni, F. Stochastic Resonance. *Rev. Mod. Phys.* **1998**, *70*, 223−287.
(94) Choi, P. J.; Cai, L.; Frieda, K.; Xie, X. S. A Stochastic Single-Molecule Event Triggers Phenotype Switching of A Bacterial Cell. *Science* **2008**, *322*, 442−445.
(95) Elf, J.; Li, G. W.; Xie, X. S. Probing Transcription Factor Dynamics at the Single-Molecule Level in A Living Cell. *Science* **2007**, *316*, 1191−1200.
(96) Sukenik, S.; Pogorelov, T. V.; Gruebele, M. Can Local Probes Go Global? A Joint Experiment−Simulation Analysis of λ_{6-85} Folding. *J. Phys. Chem. Lett.* **2016**, *7*, 1960−1965.
(97) Dave, K.; Davtyan, A.; Papoian, G. A.; Gruebele, M.; Platkov, M. Environmental Fluctuations and Stochastic Resonance in Protein Folding. *ChemPhysChem* **2016**, *17*, 1341−1348.
(98) Baldini, G.; Cannone, F.; Chirico, G. Pre-Unfolding Resonant Oscillations of Single Green Fluorescent Protein Molecules. *Science* **2005**, *309*, 1096−1100.
(99) Garai, A.; Chowdhury, D.; Ramakrishnan, T. V. Fluctuations in Protein Synthesis from A Single RNA Template: Stochastic Kinetics of Ribosomes. *Phys. Rev. E* **2009**, *79*, 011916.
(100) Hirano, Y.; Segawa, Y.; Kawai, T.; Matsumoto, T. Stochastic Resonance in A Molecular Redox Circuit. *J. Phys. Chem. C* **2013**, *117*, 140−145.
(101) Gong, Y.; Xu, B.; Ma, X.; Dong, Y.; Yang, C. Enhancement of Stochastic Resonance Induced by Either Internal or External Noise in NO Reduction on Platinum Surfaces. *J. Phys. Chem. C* **2007**, *111*, 4264−4268.
(102) Wu, M.; Wu, X.; De Camilli, P. Calcium Oscillations-Coupled Conversion of Actin Travelling Waves to Standing Oscillations. *Proc. Natl. Acad. Sci. U. S. A.* **2013**, *110*, 1339−1344.
(103) Jana, B.; Bagchi, B. Intermittent Dynamics, Stochastic Resonance and Dynamical Heterogeneity in Supercooled Liquid Water. *J. Phys. Chem. B* **2009**, *113*, 2221−2224.
(104) Chattoraj, S.; Saha, S.; Jana, S. S.; Bhattacharyya, K. Dynamics of Gene Silencing in A Live Cell: Stochastic Resonance. *J. Phys. Chem. Lett.* **2014**, *5*, 1012−1016.
(105) Chattoraj, S.; Bhattacharyya, K. Biological Oscillations: Fluorescence Monitoring by Confocal Microscopy. *Chem. Phys. Lett.* **2016**, *660*, 1−10.
(106) Dari, A.; Kia, B.; Bulsara, A. R.; Ditto, W. L. Logical Stochastic Resonance with Correlated Internal and External Noises in A Synthetic Biological Logic Block. *Chaos* **2011**, *21*, 047521−1−8.
(107) Lu, T. K.; Khalil, A. S.; Collins, J. J. Next-Generation Synthetic Gene Networks. *Nat. Biotechnol.* **2009**, *27*, 1139−1150.
(108) Debnath, M.; Ghosh, S.; Panda, D.; Bessi, I.; Schwalbe, H.; Bhattacharyya, K.; Dash, J. Small Molecule Regulated Dynamic Structural Changes of Human G-Quadruplexes. *Chem. Sci.* **2016**, *7*, 3279−3285.
(109) Debnath, M.; Ghosh, S.; Chauhan, A.; Paul, R.; Bhattacharyya, K.; Dash, J. Preferential Targeting of I-Motifs and G-Quadruplexes by Small Molecules. *Chem. Sci.* **2017**, *8*, 7448−7456.
(110) Pal, N.; Shweta, H.; Singh, M. K.; Verma, S. D.; Sen, S. Power-Law Solvation Dynamics in G-Quadruplex DNA: Role of Hydration Dynamics on Ligand Solvation inside DNA. *J. Phys. Chem. Lett.* **2015**, *6*, 1754−1760.
(111) Choi, J.; Kim, S.; Tachikawa, T.; Fujitsuka, M.; Majima, T. pH-Induced Intramolecular Folding Dynamics of i-Motif DNA. *J. Am. Chem. Soc.* **2011**, *133*, 16146−16153.
(112) Otosu, T.; Ishii, K.; Oikawa, H.; Arai, M.; Takahashi, S.; Tahara, T. Highly Heterogeneous Nature of the Native and Unfolded States of the B Domain of Protein A Revealed by Two-Dimensional Fluorescence Lifetime Correlation Spectroscopy. *J. Phys. Chem. B* **2017**, *121*, 5463−5473.
(113) Takeuchi, M.; Kajimoto, S.; Nakabayashi, T. Experimental Evaluation of the Density of Water in A Cell by Raman Microscopy. *J. Phys. Chem. Lett.* **2017**, *8*, 5241−5245.
(114) Hui, E.; Cheung, J.; Zhu, J.; Su, X.; Taylor, M. J.; Wallweber, H. A.; Sasmal, D. K.; Huang, J.; Kim, J. M.; Mellman, I.; et al. T cell Costimulatory Receptor CD28 is A Primary Target for PD-1-Mediated Inhibition. *Science* **2017**, *355*, 1428−1433.
(115) Sasmal, D. K.; Pulido, L. E.; Kasal, S.; Huang, J. Single-Molecule Fluorescence Resonance Energy Transfer in Molecular Biology. *Nanoscale* **2016**, *8*, 19928−19944.

DOI: 10.1021/acs.jpcb.7b11689
J. Phys. Chem. B 2018, 122, 3023−3036